Applied Catalysis B: Environmental 111–112 (2012) 502–508

Contents lists available at SciVerse ScienceDirect

Applied Catalysis B: Environmental

journal homepage: www.elsevier.com/locate/apcatb

Facile synthesis of pure TiO_2(B) nanofibers doped with gold nanoparticles and solar photocatalytic activities

Jesty Thomas [1], Minjoong Yoon *

Molecular/Nano Photochemistry and Photonics Lab, Department of Chemistry, Chungnam National University, Daejeon 305-764, South Korea

ARTICLE INFO

Article history:
Received 1 September 2011
Received in revised form 25 October 2011
Accepted 31 October 2011
Available online 7 November 2011

Keywords:
TiO_2(B) nanofibers
Gold nanoparticles
Doping
Solar photocatalysis
Visible light photocatalysts
Optoelectronic properties

ABSTRACT

Pure and highly crystallized gold nanoparticles-doped-TiO_2(B) nanofibers (Au-T_BNFs), with thickness of 50–200 nm and length of several microns, were successfully synthesized by combination of low-temperature (150 °C) hydrothermal reaction of titanium (IV) isopropoxide (Ti[OC_3H_7]$_4$) and sonication of the ensued precipitate with gold nanoparticles followed by post-heat treatment at 300 °C. Formation of pure TiO_2(B) was confirmed by X-ray diffraction, high resolution transmission electron microscopy and Raman spectroscopy. The UV–vis diffuse reflectance spectra (DRS) of Au–TiO_2(B) nanofibers exhibited surface-state absorption beyond 400 nm with band gap energy at 2.94 eV and broad gold plasma resonance band around 550 nm. The photoluminescence (PL) emission spectra of the Au-T_BNFs exhibited structural emission band around 410 nm with shoulders around 464 nm and 540 nm. Analysis of these optical properties revealed that the surface state absorption is attributed to the indirect transition. These results suggest that coupling of the surface charge carriers with the lattice phonon of Au-T_BNFs is so strong that the charge recombination is mostly nonradiative as supported by the significantly quenched emission of Au-T_BNFs as compared to that of free T_BNFs. These optoelectronic properties were well correlated with highly efficient solar photocatalytic activities of Au-T_BNFs for oxidation of methylene blue (MB).

1. Introduction

TiO_2 nanomaterials have attracted a great attention due to its application in photocatalysis, artificial photosynthetic systems, solar cells, etc. [1–4]. It is well known that TiO_2 nanomaterials have mostly three types of crystal phase; anatase (tetragonal), rutile (tetragonal) and brookite (orthorhombic). In addition to these phases, B-type TiO_2 (TiO_2(B)) was first synthesized in 1980 by Marchand et al. [5,6], and found in nature by Banfield et al. [7]. It has monoclinic unit cell (space group $C2/m$) with $a = 1.21787$ nm, $b = 0.37412$ nm, $c = 0.65249$ nm, and $\beta = 107.0548$, having lower density than that of the anatase, rutile, or brookite [8] with fibrous morphology [9,10]. Recently, TiO_2(B) nanoparticles were reported to exhibit the photocatalytic activity [11–14], even though their efficiency is relatively lower than that of anatase TiO_2. Also TiO_2(B) nanofibrils or nanorods have an additional advantage that they can be separated readily from a photocatalytic reaction mixture to be reused [15]. Thus, if their photocatalytic efficiency can be improved by a certain surface modification, the TiO_2(B) nanostructures would be very useful photocatalysts.

The low photocatalytic activity of the conventional TiO_2(B) nanomaterials may be due to their low purity and crystallinity although the bicrystalline phases consisting of TiO_2(B) coupled with anatase revealed higher efficiency [16,17]. Thus, many groups attempted to synthesize pure and highly crystalline TiO_2(B) by solid state reaction of TiO_2 crystals with alkali metal carbonates solution at high temperature above 800 °C [18,19]. Very recently, Chakraborty et al. [8] succeeded to synthesize pure and highly crystallized TiO_2(B) by solid state reaction of Degussa P25 with $CsCO_3$ with heat-treatment at 850 °C, and they found that their photocatlytic activities are 1.6 times bigger than those of Degussa P25. However, these high-temperature reactions require highly pressurized reactor. Alternatively hydrothermal reaction of anatase or rutile TiO_2 crystals with highly concentrated KOH or NaOH at relatively lower temperature produced TiO_2(B) nanostructures (nanotubes, nanowires, nanobelts) [11,20–22]. Sol–gel route using ionic liquids (ILs) [23] or soft chemical route [24] was presented to synthesize TiO_2(B) crystals at low-temperature (100 °C) at ambient pressure. Nevertheless, these low-temperature processes provide less crystallized TiO_2(B) with low yield (60–90 wt.%), because B-phase is easily converted to anatase at a relatively low temperature [20,25]. Thus, there still requires more facile route to synthesize pure and highly crystallized TiO_2(B) nanostructures at low temperature.

* Corresponding author. Tel.: +82 42 821 6546; fax: +82 42 823 7008.
E-mail address: mjyoon@cnu.ac.kr (M. Yoon).
[1] Present address: Department of Chemistry, K.E College, Kottayam, India.

0926-3373/$ – see front matter © 2011 Elsevier B.V. All rights reserved.
doi:10.1016/j.apcatb.2011.10.039

The photocatalytic activities of TiO_2(B) nanocrystals have been usually investigated under UV light irradiation because most of the TiO_2(B) nanocrystals have a band gap energy of 3.2 eV corresponding to UV absorption. This practically rules out the use of sunlight as energy source in solar photocatalysis and its application to solar fuels, and no investigation has been done for the solar photocatalytic properties of TiO_2(B) nanocrystals. In order to use TiO_2(B) nanocrystals as solar photocatalysts, TiO_2(B) nanocrystals need to be intrinsically or extrinsically modified as in the case of anatase TiO_2 nanocrystals [3,26–29] so that they can harvest visible light. Such modifications are known to improve the photocatalytic efficiency by the charge separation through reduction of exciton recombination.

In this work we synthesized pure and highly crystallized gold-doped TiO_2(B) nanofibers by simple hydrothermal reaction of a precursor, titanium (IV) isopropoxide ($Ti[OC_3H_7]_4$) instead of TiO_2 powder at 150 °C followed by sonication of the ensued precipitate low-temperature (300 °C) calcinations with gold nanoparticles. Thereafter, we investigated their optoelectronic properties by using UV–vis diffuse reflectance absorption and photoluminescence spectroscopic techniques, correlating them to their photocatalytic activities measured under visible light and solar irradiation.

2. Experimental

2.1. Materials

Analytical grade titanium (IV) isopropoxide ($Ti[OC_3H_7]_4$), for the synthesis of TiO_2(B) was purchased from Sigma–Aldrich, methylene blue was obtained from Rankem. Chloroauricacid ($HAuCl_4$), sodium hydroxide (NaOH), D-glucosamine hydrochloride used for the synthesis of gold nanoparticles were purchased from Aldrich chemicals. All these chemicals were used without further purification.

The gold nanoparticles used for doping into TiO_2(B) nanofibers were synthesized in a single step from chloroauricacid ($HAuCl_4$) by chemical reduction technique employing a biologically active molecule D-glucosamine which is different from usual stabilizing agent like polyethyleneglycol [30] or surfactants [31]. Stock solutions of $HAuCl_4$ (0.2 mM) and glucosamine hydrochloride (10.0 mM) were prepared in doubly distilled water. Au^{3+} solution (30.0 ml) was mixed with aliquot amounts of glucosamine by adding micro liter quantities of stock solution. The mixture was stirred for 5 min. The formation of gold nanoparticles was identified by a visual color change from light yellow to reddish wine color with evolution of a new band at 521 nm in the absorption spectrum (Fig. 1a) which is the characteristic plasma resonance for gold nanoparticles [32,33]. According to Mie's theory and Maxwell's equation, the surface plasma absorption and the plasma bandwidth are size-dependent with the metallic particles in the solution. This peak value represents the average size of gold nanoparticles in the solution is around 5 nm [34] as confirmed by TEM image (Fig. 1b). These results show that gold nanoparticles are well stabilized, indicating good ability of D-glucosamine as an excellent reducing and stabilizing agent.

2.2. Synthesis of free and gold-doped TiO_2(B) nanofibers

TiO_2(B) nanofibers were synthesized through formation of trititanate nanofibers by hydrothermal reaction using liquid titanium (IV) isopropoxide as starting materials as shown in Scheme 1. 30.0 ml of 10.0 M NaOH solution was added to 7.0 ml titanium (IV) isopropoxide with constant stirring to get white precipitates. The stirring was continued for 2.0 h and was transferred into a stainless steel Teflon-autoclave (100 ml) and kept at 150 °C for 48 h. After the completion of the autoclaving treatment, it was filtered, washed with water and acetone. Then the filtered solid is stirred with 0.1 M HCl to remove the intercalated Na^+ which is essential to improve the stability and the crystallinity of the sample [35], which was again washed with water and acetone and then dried at 80 °C to produce titanate ($H_3Ti_3O_7$) nanofibers (TiNFs). When the aqueous

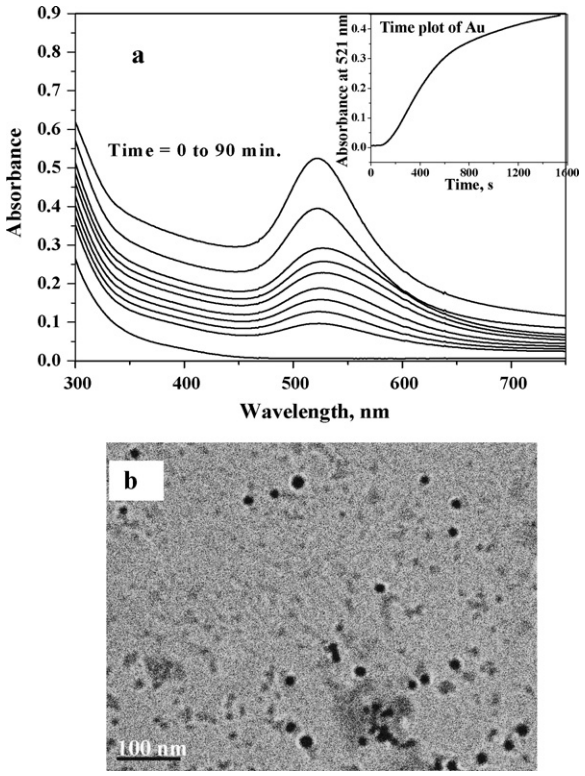

Fig. 1. (a) Absorption spectra of gold nanoparticles recorded at different time intervals, plot of evolution of absorbance at 521 nm as a function of time (inset) (b) TEM of synthesized gold nanoparticles.

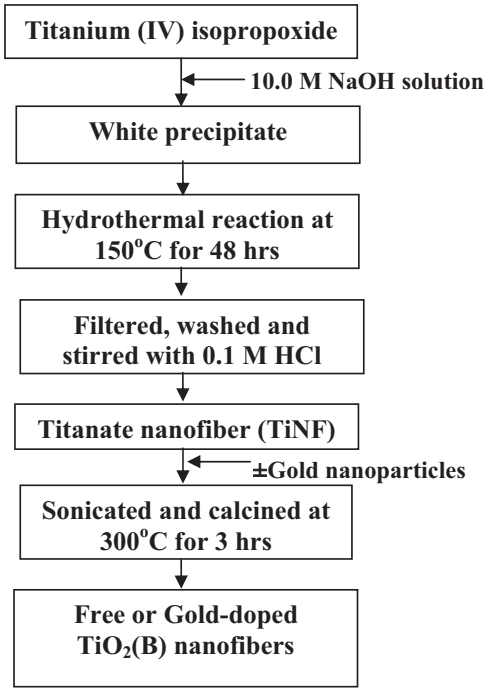

Scheme 1. Synthetic route of TiO_2(B) nanofibers.

dispersion of the TiNFs was further sonicated and calcined at 300 °C for 3 h, free TiO_2(B) nanofibers (T_BNFs) could be obtained. On the other hand, the gold-doped TiO_2(B) nanofibers (Au-T_BNFs) could be obtained by sonicating the aqueous mixture dispersion of the TiNFs and the synthesized gold nanoparticles (0.1 mass% with respect to TiNFs), followed by drying at 80 °C and calcinated at 300 °C for 3 h.

For comparison purpose, anatase TiO_2 nanoparticles (TNPs) were also synthesized by the similar process using distilled water without treatment with 10 M NaOH and 0.1 M HCl.

2.3. Structural characterization

SEM images of as-prepared samples were obtained by using a field emission scanning electron microscope (FE-SEM, Jeol JSM 6500 FE). Transmission electron microscopic characterization was carried out by using a Jeol JEM-3010 transmission electron microscope. The BET specific surface area of the powders was measured via Brunauer–Emmett–Teller (BET) technique measuring nitrogen adsorption–desorption isotherm, using a surface area and porosity analyzer (Micromeritics, Gemini, USA). The X-ray diffraction patterns (XRD) of the synthesized samples were obtained on a Brucker D8, Advance diffractometer using Cu Kα radiation.

2.4. Spectroscopic measurements

Raman spectra were measured on MOF-IR 550 spectrometer. The diffused reflection spectra (DRS) of the samples were performed using a UV-2450 Shimadzu UV–visible spectrophotometer. The photoluminescence (PL) spectral measurements were made using Shimadzu RF-5301 spectrofluorometer.

2.5. Measurement of photocatalytic activities

The photocatalytic activities of the synthesized samples were assessed by measurement of degradation of methylene blue (MB) under solar and visible light irradiation. For a typical photocatalytic experiment, 1.5 mg of synthesized samples (TNP, T_BNF, Au-T_BNF) were suspended separately in 7.0 ml aqueous solution of 20 ppm MB in a Pyrex test tube. The resulting suspension was equilibrated by stirring in the dark for 30 min. After equilibration, the sample solution was irradiated with solar simulator (Asahi Spectra MAX-302 xenon light source attached with A.M. 1.5 filter) at room temperature with oxygen bubbling. Visible light irradiation was also carried by using the same light source but with UV cut-off filter under the same conditions. The samples were withdrawn at different time intervals and centrifuged at 3000 rpm to separate the nanofibers. The absorbance change of MB was measured at 660 nm using a UV-3101 PC UV–vis–NIR Shimadzu scanning spectrophotometer. It was confirmed as a control that no detectable degradation of MB occurs without TiO_2 or irradiation alone.

3. Results and discussion

3.1. Structural characterization

XRD patterns of the synthesized free T_BNF and Au-T_BNF are shown in Fig. 2, and compared with those of TNP and TiNFs. The XRD pattern of TiNF exhibits typical distinguishable peaks at (2 0 0), (1 1 0) and (0 2 0) without any peaks of anatase phase (JCPDS, No. 21-1272), confirming pure and highly crystalline hydrogen titanates with formula $H_2Ti_nO_{2n+1}$ ($3 \le n \le 6$) like $H_2Ti_3O_7$ [2,36,37], which are the essential requirements for the prerequisite for the synthesis of pure TiO_2(B) phase [8]. The major XRD peaks of TiNF were observed to be shifted to higher angle and broader upon sonication followed by calcination at 300 °C (Fig. 2, T_BNF), being attributed to dimensional confinement effect caused by decrease of

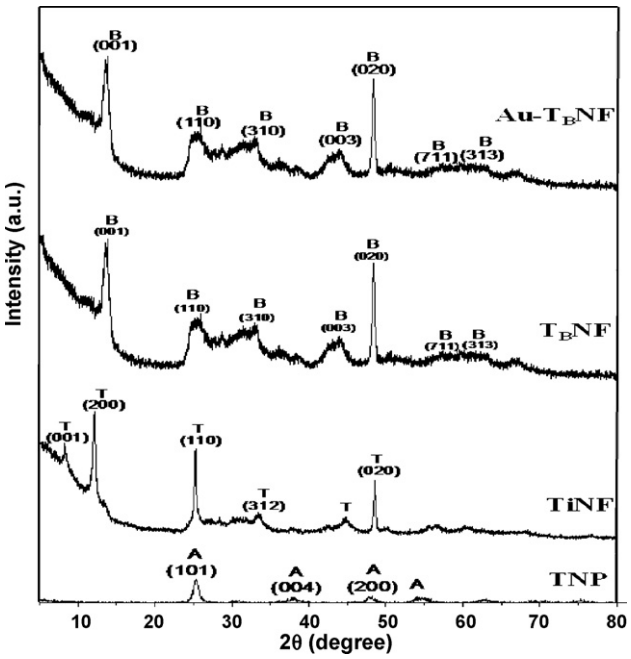

Fig. 2. XRD patterns of as-synthesized TNP, TiNF, T_BNF and Au-T_BNF.

interlayer spacing (crystal size decrease, (*vide infra*)) through dehydration in the heat treatment [38]. The shifted XRD pattern was in good agreement with TiO_2(B) datasheet (ICDD # 35-0088) [24], and no peaks for both anatase and rutile phases were observed within the XRD detection limit. These results support that TiNF was purely converted to highly crystalline B-phase nanofiber (T_BNF) [39–42]. The XRD pattern of T_BNF was not changed even after forming Au-doped T_BNF (Au-T_BNF), even though diffraction peaks of gold (2 0 0) and (2 2 0) at $2\theta = 44°$ and 64° (JCPDS 4–0784) could not be detected because of the very small amount of gold. This indicates that the B-phase is not changed by gold doping.

Morphologies and crystalline states of TiNF, T_BNF and Au-T_BNF were identified by measurement of FE-SEM and TEM images. Fig. 3 shows the FE-SEM images of fibrous morphologies having thickness of 50–200 nm and length of a few to several tens microns. The SEM images of all the three samples are the same, indicating that calcination or introduction of gold nanoparticle does not alter the morphologies although the crystalline phase is changed from titanate to TiO_2(B). Fig. 4a shows the TEM images of TiNFs with well-defined selected area electron diffraction (SAED) pattern of (2 0 0) plane. The uniform lattice fringes were observed over a wide surface layer as shown in the high resolution TEM (HRTEM) images (Fig. 4b) with the distance between lattice fringes of 1.08 nm. These observations confirm the morphology of single crystalline nanofiber. The TEM images of Au-T_BBFs (Fig. 4c) show the similar SAED pattern which were fully indexed to the monoclinic C2/m space group of TiO_2(B), supporting that Au-T_BNFs are highly crystalline. The lattice space (Fig. 4d) was reduced to 0.643 nm from that of TiNF, which was identified to be $d_{0\,0\,1}$ and the same as that of free T_BBF (Fig. 4e and f).

Fig. 5 shows Raman spectra of TiNF, Au-T_BNF and anatase TNP. The spectrum of TiNF exhibits Raman bands for $H_2Ti_3O_7$ in agreement with previous studies [43,44], representing different titanium and oxygen stretching vibrations in the octahedral TiO_6 [36]. Au-T_BNF obtained from TiNF exhibited different Raman spectral peaks which matches with the reported bands of TiO_2(B) [23,36]. In both Raman spectra, the characteristic band (around 920 cm^{-1}) for stretching vibration of short Ti–O bonds coordinated with sodium ions was not observed, indicating complete removal of Na^+ ions

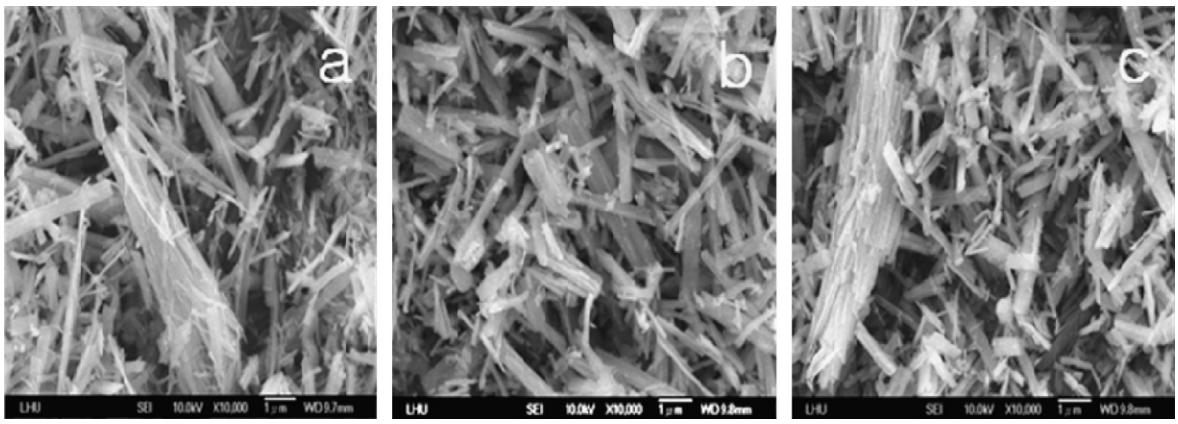

Fig. 3. FE-SEM images of (a) TiNF, (b) T_BNF and (c) Au-T_BNF.

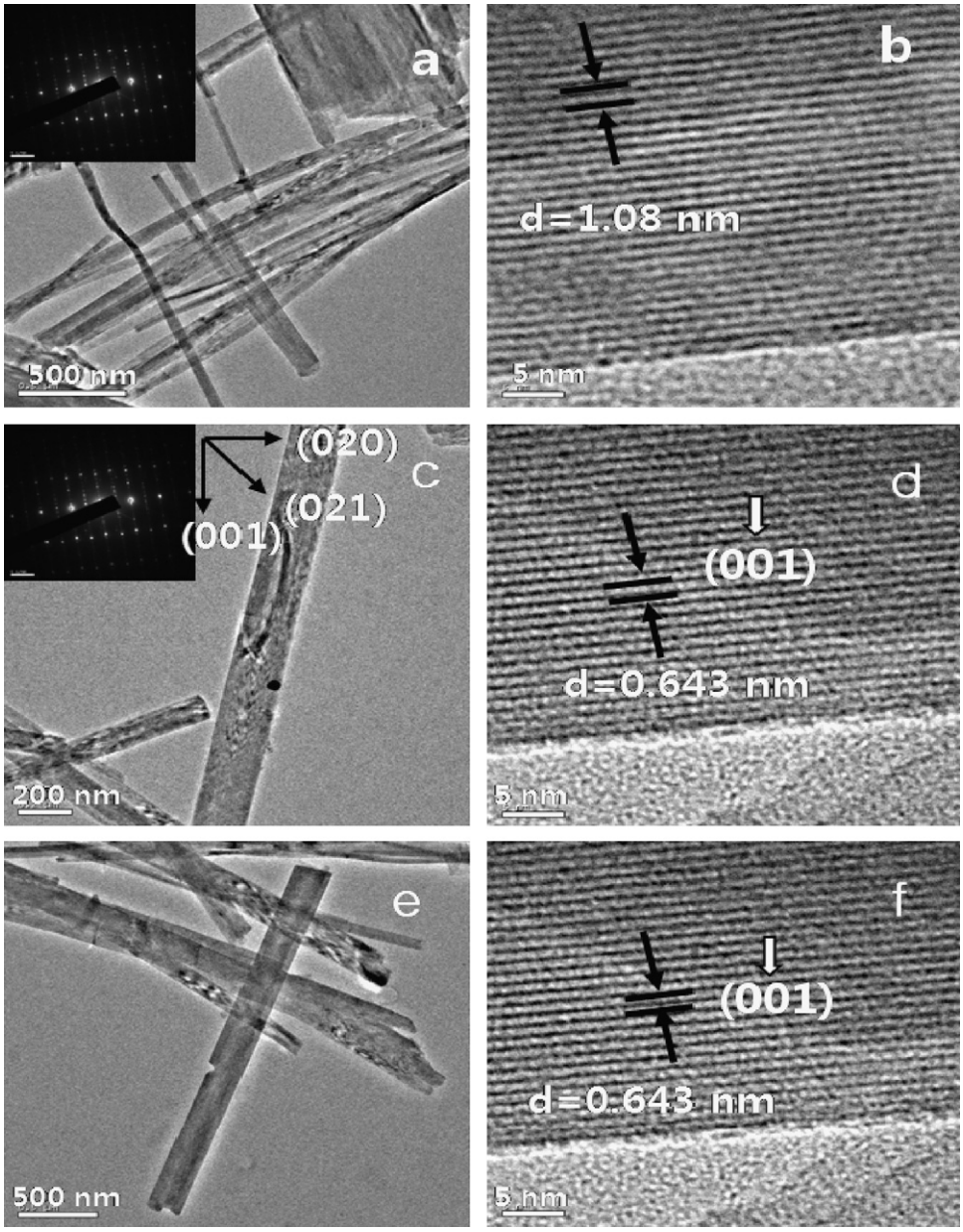

Fig. 4. TEM image of (a) TiNF with a SAED pattern (inset), (b) HRTEM of TiNF, (c) TEM image of Au-T_BNF with a SAED pattern (inset), (d) HRTEM of Au-T_BNF, (e) TEM image of T_BNF, (f) HRTEM of T_BNFs.

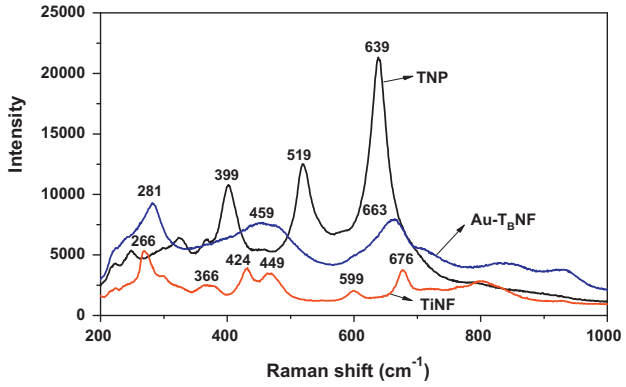

Fig. 5. Raman spectra of TNP, TiNF, and Au-T_BNF.

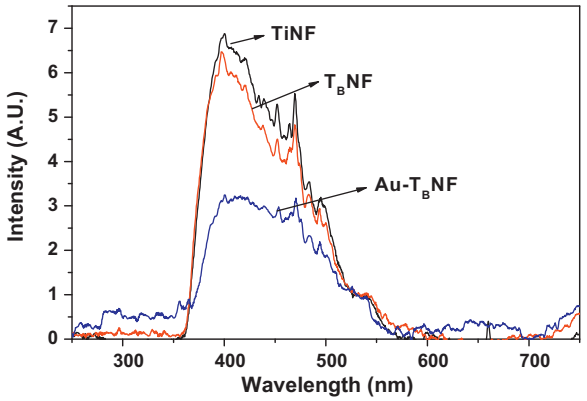

Fig. 7. Photoluminescence emission spectra of TiNF, T_BNF and Au-T_BNF (λ_{ex} = 380 nm).

from TiNF and Au-T_BNF in contrary to the report by Papp et al. [42]. It is also noteworthy that both Raman spectral peaks are completely distinguishable from those for anatase TNP. These results support again that both TiNF and Au-T_BNF are pure without anatase phase in contrast to the previous reports [26,27].

The BET surface areas of the synthesized samples, TiNF, T_BNF and Au-T_BNF were determined to be 14.7, 36.9 and 37.1 m^2/g, respectively. These values are much smaller than that of anatase TNP (119.5 m^2/g) but about 2 times bigger than other conventional TiO_2 (B) nanostructures [8,36,37]. The particle size of the samples were calculated from surface area using Eqn. $D_{BET} = 6000/\rho S$, where D_{BET} is the average nanoparticle size (nm), ρ is the powder density (g/cm^3), S is the specific surface area (m^2/g). According to this calculation, the average particle sizes of T_BNF and Au-T_BNF is 51.4 and 51.2 nm, which are much smaller than that of 129 nm. These results support that the broadening of XRD and Raman peaks (*vide supra*) is due to dimensional confinement as reported by Armstrong et al. for TiO_2(B) nanotubes, nanowires, etc. [40].

3.2. Optical properties

Fig. 6 shows the DRS of the free T_BNF and Au-T_BNF. The band gap energy estimated from the absorption edge of T_BNF was observed to be red-shifted from that of anatase TNP (390 nm, 3.18 eV) toward visible region, indicating possibility of slight visible light surface absorption by T_BNF. Au-T_BNF also showed the red-shifted band gap as in the case of free T_BNF, but its visible absorption band in 500–700 nm region is highly enhanced and broader, which is originated from to the plasma resonance of gold nanoparticles [45,46]. It is noteworthy that the absorption maximum of gold plasma resonance band in Au-T_BNF was observed to be red-shifted by about 30 nm from that of free gold nanoparticles, indicating gold nanoparticles-doped in TiO_2(B) lattice environment. The nature of the band gap (either an indirect or a direct transition) was determined by using the power expression; $(\alpha h\upsilon)^n = K_{i,d}(h\upsilon - E_g)$, where E_g is the band gap energy, α is the absorbance, $h\upsilon$ is the absorption energy, and $K_{i,d}$ is the absorption constant for an indirect (subscript i) or direct (subscript d) transition corresponding to 1/2 and 2 for n, respectively [38]. Inset of Fig. 6 shows the linear plots of $(\alpha h\upsilon)^{1/2}$ against absorption energy ($h\upsilon$) of T_BNF and Au-T_BNF, from which the correct E_g was estimated to be 3.04 eV and 2.94 eV for T_BNF and Au-T_BNF, respectively. These band gap energies are in agreement to the onset energy observed in the absorption spectra above, confirming that the band gap is attributed to the indirect transition. This is in contrast to the direct electronic transition dominant for the band gap nature of anatase TiO_2 nanoparticles [2,47], implying that the interaction between the exciton and lattice phonon on the surface of T_BNFs is so strong that density of surface states in T_BNFs is relatively high [48]. Thus, it can be expected that the electron and hole can be effectively trapped on surface states so that the charge separation would be effective. It is usually known that the effective separation of the trapped charges result in generation of strong surface-emission with weak band-edge emission [2,49].

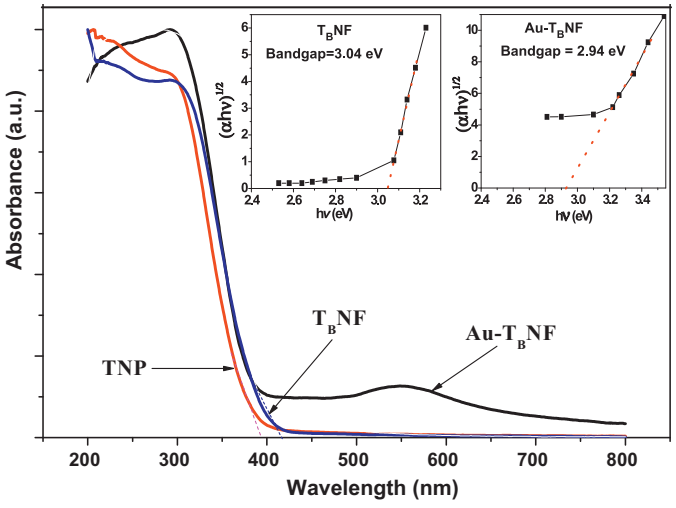

Fig. 6. Diffuse reflectance absorption spectra of TNP, T_BNF and Au-T_BNF. Plot of $(\alpha h\upsilon)^{1/2}$ versus photon energy ($h\upsilon$) of Au-T_BNF (inset).

Fig. 7 shows the PL emission spectra of TiNF, T_BNF and Au-T_BNF measured under the same condition with an excitation wavelength of 380 nm. Both TiNF and T_BNF exhibit a strong structural surface-emission band around 410 nm with broad band beyond 450 nm down to 600 nm, confirming the presence of several surface states. It should be noted that such strong surface-emission was not observed from the anatase TNP which generates only weak band-edge emission. Thus, the strong emission of T_BNF should be attributed to the recombination of electron–hole pair trapped on the surface states. Interestingly the surface emission of T_BNF was significantly quenched upon formation of Au-T_BNF, indicating that the doped Au-nanoparticles play an important role in recombination of the surface state-trapped charge carriers. Actually gold nanoparticles are supposed to scavenge the photoinduced electrons of TiO_2(B), leading to the reduction of electron–hole recombination so that the surface emission is quenched. These results suggest that the electrons trapped in gold nanoparticles may be subsequently transferred to the surrounding O_2 to form active oxygen radical species for improved photocatalytic action [50,51].

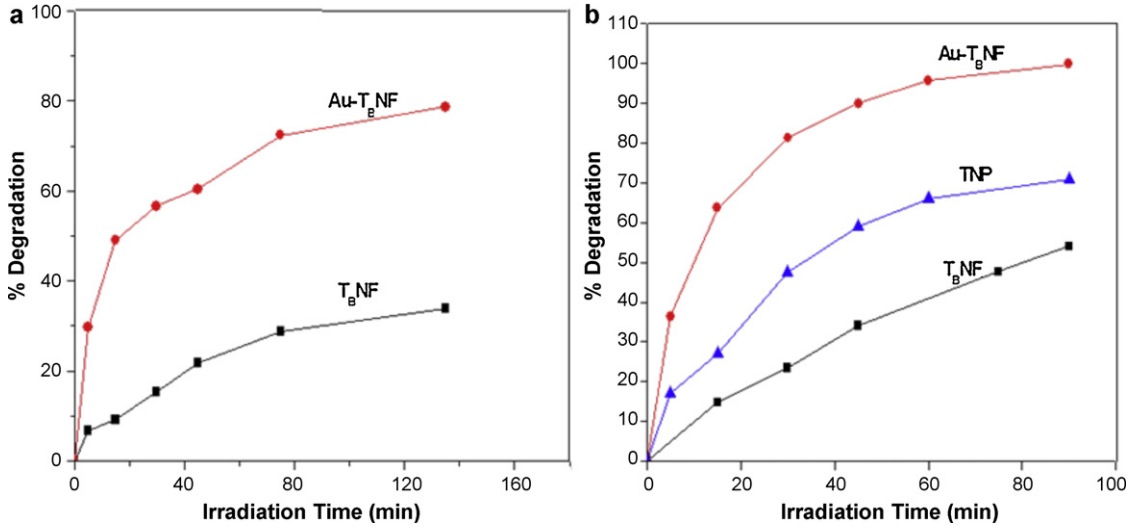

Fig. 8. Photocatalytic decomposition of MB with T_BNF and Au-T_BNF upon irradiation with visible light (>400 nm) (a) and with solar light (A.M. 1.5) (b).

3.3. Photocatalytic activities

The well-separation of surface charge carriers and visible light absorption imply that Au-T_BNF would be very useful for highly improved solar photocatalysts and solar cells. To confirm this implication, the photocatalytic activities of free T_BNF and Au-T_BNF were investigated under visible light and solar illumination by monitoring the decomposition of MB in water. Fig. 8a shows % degradation of MB as a function of irradiation with visible light (>400 nm) in the presence of T_BNF and Au-T_BNF. About 30% of MB was observed to be photocatalytically decomposed in 120 min with free T_BNF while no decomposition was observed with anatase TNP. This may be because T_BNF has slightly stronger absorption of visible light beyond 400 nm than TNP. Such visible light photocatalytic effects were observed to be significantly enhanced by using Au-T_BNF. This enhancement may be due to not only stronger visible light absorption but also the further charge separation between the surface state and Au as discussed above.

Such photocatalytic decomposition of MB was also examined in the presence of TNP, T_BNF and Au-T_BNF upon illumination with solar simulator (A.M. 1.5). As shown in Fig. 8b, the solar photocatalytic degradation of MB with Au-T_BNF was observed to be 100% completed in 90 min, implying that the solar photocatalytic efficiency of Au-T_BNF is much higher than that of TNP or T_BNF. The first-order kinetic model derived from the Langmuir–Hinshelwood kinetic equation was used to determine the photocatalytic efficiency of the synthesized samples (TNP, T_BNF and Au-T_BNF) under solar light irradiation and is given in Fig. 9. The first-order rate constant (k), equivalent to the slope of the linear regression was

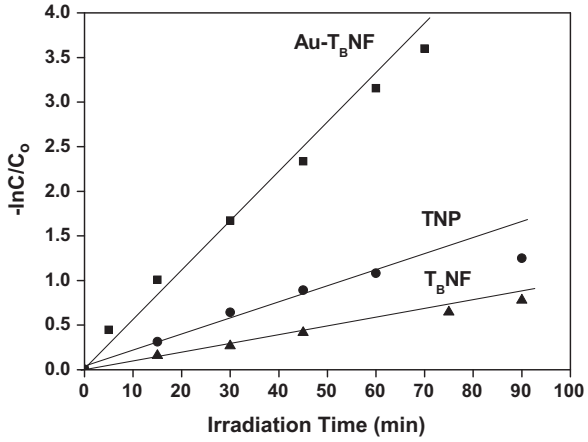

Fig. 9. Photocatalytic degradation kinetics of TNP, T_BNF and Au-T_BNF under solar light irradiation.

determined to be 0.019, 0.010, and 0.056 min^{-1}, respectively for TNP, T_BNF and Au-T_BNF.

Interestingly, in contrast to the higher visible light photocatalytic activity of T_BNF than that of TNP, solar photocatalytic activity of TNP is higher than that of T_BNF. This implies that the high UV-photocatalytic activity of the anatase TiO_2 is still superior to that of TiO_2(B) nanofiber which absorbs visible light weakly, because small fraction of UV light is available in solar light. Nevertheless it is evident that the solar photocatalytic activity of Au-T_BNF is 3

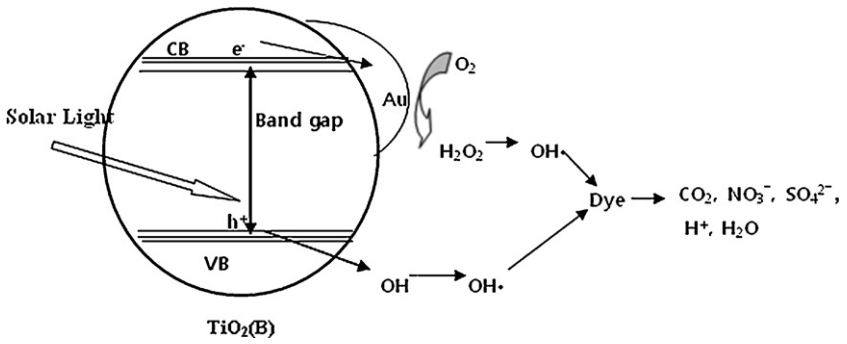

Scheme 2. Mechanism of solar photocatalytic decomposition of MB with Au-T_BNF.

times higher than that of anatase TNP even though BET surface area of Au-T_BNF is much smaller than that of TNT. This indicates that both high visible light absorption and well-separated charge carriers play a critical role in enhancement of the photocatalytic activity of Au-T_BNF as shown in Scheme 2. As discussed above, TiO_2(B) nanofibers have high density of surface states which can trap UV or visible light-induced electron and holes separately. Thus, the surface state-trapped electron can be efficiently transferred to Au which relay electron to form an oxidant radical $OH^\bullet$ by interacting with O_2 in water while the hole can interact with OH^- to form the $OH^\bullet$.

4. Conclusions

Pure and highly crystallized TiO_2(B) nanofibers doped with gold nanoparticles (Au-T_BNF) were synthesized by combination of low-temperature (150 °C) hydrothermal reaction and sonication followed by calcination (300 °C), employing titanium (IV) isopropoxide ($Ti[OC_3H_7]_4$) and gold nanoparticles. It was found that the gold nanoparticles-doped TiO_2(B) nanofibers absorb visible light strongly in wide range. The photoluminescence studies of free TiO_2(B) nanofibers (T_BNF) implied presence of high density of surface states to trap the charge carriers separately. The surface state-trapped charge carriers were found to be efficiently transferred to gold doped on the surface as proved by 3 times higher in the solar photocatalytic efficiency of Au-T_BNF than that of anatase TNPs or free T_BNF. The present study suggests that Au-T_BNF would be very useful in an environmentally sustainable photocatalytic treatment process for the degradation of environmental pollutants using sunlight.

Acknowledgements

This work was financially supported by National Research Foundation of Republic of Korea (NRF 2010-0002880) and the Brain Korea 21 (BK21) program of the Korea Ministry of Education, Science and Technology for the postdoctoral fellowship (Jesty Thomas).

References

[1] A. Hagfeldtt, M. Grätzel, Chem. Rev. 95 (1995) 49.
[2] M. Yoon, M. Seo, C. Jeong, J.H. Jang, K.S. Jeon, Chem. Mater. 17 (2005) 6069.
[3] K.P. Sreenivasan, Y.M. Lee, M. Yoon, Electrochem. Commun. 11 (2009) 1211.
[4] M.A. Fox, M.T. Dulay, Chem. Rev. 93 (1993) 341.
[5] R. Marchiand, L. Brohan, M. Tournoux, Mater. Res. Bull. 15 (1980) 1129.
[6] M. Tournoux, R. Marchand, L. Brohan, Prog. Solid State Chem. 17 (1986) 33.
[7] J. Banfield, D. Veblen, D. Smith, Am. Mineral. 76 (1991) 343.
[8] A.K. Chakraborty, Q. Zhang, S.Y. Chai, C. Lee, S.Y. Park, D.J. Jang, W.I. Lee, Appl. Catal. B: Environ. 93 (2010) 368.
[9] S. Yin, Y. Fujishiro, J. Wu, M. Aki, T. Sato, J. Mater. Proc. Technol. 137 (2003) 45.
[10] G. Armstrong, A.R. Armstrong, P.G. Bruce, P. Reale, B. Scrosati, Adv. Mater. 18 (2006) 2597.
[11] H.L. Kuo, C.Y. Kuo, C.H. Liu, J.H. Chao, C.H. Lin, Catal. Lett. 113 (2007) 7.
[12] K. Yamamoto, H. Shimoita, K. Tomita, K. Fujita, M. Kobayashi, V. Petrykin, M. Kakihana, J. Ceram. Soc. Jpn. 117 (2009) 347.
[13] X. Zhang, J.H. Pan, A.J. Du, P.F. Lee, D.D. Sun, J.O. Leckie, Chem. Lett. 37 (2008) 424.
[14] W. Li, Y. Bai, C. Liu, Z. Yang, X. Feng, X. Lu, N.K. Van Der Laak, K.Y. Chan, Environ. Sci. Technol. 43 (2009) 5423.
[15] Y. Yu, D. Xu, Appl. Catal. B: Environ. 73 (2007) 166.
[16] W. Li, C. Liu, Y. Zhou, Y. Bai, X. Feng, Z. Yang, L. Lu, X. Lu, K.Y. Chan, J. Phys. Chem. C 112 (2008) 20539.
[17] D. Yang, H. Liu, Z. Zheng, Y. Yuan, J. Zhao, E.R. Waclawik, X. Ke, H. Zhu, J. Am. Chem. Soc. 131 (2009) 17885.
[18] A. Kudo, T. Kondo, J. Mater. Chem. 7 (1997) 777.
[19] M. Zukalová, M. Kalbáč, L. Kavan, I. Exnar, Chem. Mater. 17 (2005) 1248.
[20] A.R. Armstrong, G. Armstrong, J. Canales, P.G. Bruce, Angew. Chem. Int. Ed. 43 (2004) 2286.
[21] Y.V. Kolenko, K.A. Kovnir, A.I. Gavrilov, A.V. Garshev, J. Frantti, O.I. Lebedev, B.R. Churagulov, G.V. Tendeloo, M. Yoshimura, J. Phys. Chem. B 110 (2006) 4030.
[22] D.V. Bavykin, J.M. Friedrich, F.C. Walsh, Adv. Mater. 18 (2006) 2807.
[23] H. Kaper, S. Sallard, I. Djerdj, M. Antonietti, B.M. Smarsly, Chem. Mater. 22 (2010) 3502.
[24] M. Estruga, C. Domingo, J.A. Ayllón, Mater. Lett. 64 (2010) 2357.
[25] S. Pavasupree, Y. Suzuki, S. Yoshikawa, R. Kawahat, J. Solid State Chem. 178 (2005) 3110.
[26] W.T. Geng, K.S. Kim, Solid State Commun. 129 (2004) 741.
[27] P.D. Cozzoli, R. Comparelli, E. Fanizza, M.L. Curri, A. Agostiano, D. Laub, J. Am. Chem. Soc. 126 (2004) 3868.
[28] K.S. Mayya, D.I. Gittins, F. Caruso, Chem. Mater. 13 (2001) 3833.
[29] M. Haruta, Catal. Today 36 (1997) 153.
[30] C. Burda, X. Chen, R. Narayanan, M.A. El-Sayed, Chem. Rev. 105 (2005) 1025.
[31] C.H. Su, P.L. Wu, C.S. Yeh, J. Phys. Chem. B 107 (2003) 14240.
[32] N.K. Chaki, K. Vijaymohanan, J. Phys. Chem. B 109 (2005) 2552.
[33] J. Sharma, J.P. Vivek, K. Vijaymohanan, J. Nanosci. Nanotechnol. 6 (2006) 3464.
[34] F. Chun, G. Lina, Y. Dong, H. Jianhua, L. Guolin, H. Xiaoyu, Polymer 50 (2009) 3990.
[35] L.Q. Weng, S.H. Song, S. Hodgson, A. Baker, J. Yu, J. Eur. Ceram. Soc. (2006) 1405.
[36] Y.V. Kolen'ko, K.A. Kovnir, A.I. Gavrilov, A.V. Garshev, J. Frantti, O.I. Lebedev, B.R. Churagulov, G. Van Tendeloo, M. Yoshimura, J. Phys. Chem. B 110 (2006) 4030.
[37] S. Pavasupree, Y. Suzuki, S. Yoshikawa, R. Kawahata, J. Solid State Chem. 178 (2005) 3110.
[38] R. Yoshida, Y. Suzuki, S. Yoshikawa, Mater. Chem. Phys. 91 (2005) 409.
[39] L. Cui, F. Huang, M. Niu, L. Zeng, J. Xu, Y. Wang, J. Mol. Catal. A: Chem. 326 (2010) 1.
[40] G. Armstrong, A.R. Armstrong, J. Canales, P.G. Bruce, Chem. Commun. (2005) 2454.
[41] A. Riss, T. Berger, H. Grothe, J. Bernardi, O. Diwald, E. Knozinger, Nano Lett. (2007) 433.
[42] S. Papp, L. Korosi, V. Meynen, P. Cool, E.F. Vansant, I. Dekany, J. Solid State Chem. 178 (2005) 1614.
[43] Y. Wu, M. Long, W. Cai, S. Dai, C. Chen, D. Wu, J. Bai, Nanotechnology 20 (2009) 185703.
[44] L.L. Costa, A.G.S. Prado, J. Photochem. Photobiol. A: Chem. 201 (2009) 45.
[45] S.V. Awate, R.K. Sahu, M.D. Kadgaonkar, R. Kumar, N.M. Gupta, Catal. Today 141 (2009) 144.
[46] R. Ma, T. Sasaki, Y. Bando, J. Am. Chem. Soc. 126 (2004) 10382.
[47] N. Serpone, D. Lewless, R. Khairutdinov, J. Phys. Chem. 99 (1995) 16646.
[48] Z.P. Wang, W.M. Cai, X.T. Hong, X.L. Zhao, F. Xu, C.G. Cai, Appl. Catal. B. Environ. 57 (2005) 223.
[49] Y. Wang, N. Herron, J. Phys. Chem. 95 (1991) 525.
[50] F.B. Li, X.Z. Li, M.F. Hou, K.W. Cheah, W.C.H. Choy, Appl. Catal. A: Gen. 285 (2005) 181.
[51] B. Zhu, Z. Sui, S. Wang, X. Chen, S. Zhang, S. Wu, W. Huang, Mater. Res. Bull. 41 (2006) 1097.